Visual Abstract

Behavior of Zr–1Nb alloy in coarse- and ultrafine-grain states under laser-induced shock wave loading

Dmitry Ledon, Aleksandr Balakhnin, Sergey Uvarov, Irina Bannikova, Yuriy Bayandin, Oleg Naimark
Institute of Continuous Media Mechanics of Ural branch of RAS, Russia
ledon@icmm.ru http://orcid.org/0000-0003-1541-2246
balakhnin.a@icmm.ru http://orcid.org/0009-0001-4127-429X
usv@icmm.ru http://orcid.org/0000-0002-7538-0971
malgacheva@icmm.ru http://orcid.org/0000-0002-1344-1265
buv@icmm.ru http://orcid.org/0000-0002-1824-1940
naimark@icmm.ru http://orcid.org/0000-0001-6537-1177

ABSTRACT. The work is devoted to the study of the Zr-1Nb alloy in coarse-grained and ultrafine-grained states under laser-induced shock-wave loading. This material is of interest due to the application for the manufacture of shells for fuel elements of nuclear reactors. The properties of this alloy in the ultrafine-grained state is attracted for the reliability improvement of fuel rods in wide range of load intensity. Shock wave loading was carried out using a Beamtech SGR-Extra-10 high-energy nanosecond laser. The free surface velocity profiles were registered by the VISAR system. Mechanical characteristics are obtained using velocity profiles. It is shown that the spall strength and dynamic elastic limit for the coarse-grained state are higher than for the ultrafine-grained state. In general, the Zr-1Nb alloy in the ultrafine-grained state is more susceptible to spall fracture, including laser shock peening. Numerical simulation of the process under study has been carried out using statistically based nonlinear model of solid with defects and finite element method to describe the deformation behavior and fracture of the material under shock-wave loading. Simulation results are qualitatively consistent with experiments in the prediction of the conditions of spall failure.

KEYWORDS. Zr-1Nb alloy, Shock-wave loading, Ultrafine-grain state, Structural studies, Spall fracture.

Citation: Ledon, D., Balakhnin, A., Uvarov, S., Bannikova, I., Bayandin, Y., Naimark, O., Behavior of Zr–1Nb alloy in coarse- and ultrafine-grain states under laser-induced shock wave loading, Frattura ed Integrità Strutturale, 66 (2023) 164-177.

Received: 12.07.2023
Accepted: 11.08.2023
Online first: 15.08.2023
Published: 01.10.2023

INTRODUCTION

Laser shock peening (LSP) is generated by a laser beam of high energy intensity and short pulse width with ablative coating irradiation and is considered as effective treatment of metallic surface layer by Laser Shock Wave (LSW) [1-5]. This loading provides the improvement of fatigue life and the resistance of foreign object damage (FOD) [6-8]. Nanosecond duration of laser-beam induced intensive pulse under LSP conditions leads to specific mechanisms of structure evolution, when the shock wave (SW) exceeds the Hugoniot elastic limit (HEL) and the micro-structure of the surface layer changes resulting multiscale damage and residual stress [9-12]. The internal damage as the precursor of spall fracture is induced by the interaction of a compressive and tensile waves [13].

LSP treatment reveals problems being applied to thin structures, for instance, the thin edge of aviation blades [14], when spall fracture occurs near the free surface of the specimen due to the damage accumulation in the rarefaction wave that leads to rapidly decrease the fatigue life of the components. This phenomenon has been observed after LSP experiments by [15-18] for aluminum alloys and by [19-21] for titanium alloys due to the nucleation, growth and coalescence of the micro-voids.

The laser-induced spall fracture of pure aluminum, copper and iron were studied by Eliezer [22] and Boustie [23]. Righi [24] reported the influence of the grain size and the strain rate on spall strength in pure iron through LSW treatment. Zhang [25] established the links of the spall fracture characteristics of 90W–Ni– Fe alloy with the nucleation of initial damage during laser-induced shock load. Wu [26] reported the over peening effect due to internal spall fracture of medium thick Al7050 plates with continued multiple shocks LSP.

The understanding of mechanisms of LSW treatment of titanium alloys represents the interest for aeroengines applications (fan blades, components of pressure compressors), due to their mechanical properties, including the resistance to fatigue, high temperature and corrosion [27]. Titanium components are frequently subjected also to extreme conditions, such as foreign object damage [28, 29], which reduce the service life and affect the reliability of aero engines. The laser shock peening (LSP) being the surface layer treatment technique by nanosecond pulse laser could provide the microstructure the delaying the crack initiation and decelerating the crack propagation rate. It was reported, that the fatigue striation spacing in LSP treated specimen is narrower than unpeened ones [30] and the fatigue crack propagation (FCP) rate in the initial fatigue crack growth stage of 6061-T6 aluminum alloy is decreased.

LSP induced deceleration in the FCP rate during the propagation in AA2024-T351 aluminum alloy was studied by Kashaev [31], but the structural explanation of the nature of deceleration zone on the fracture surface remains unclear. Therefore, it is of necessity to understand this phenomenon to develop models of crack advance with LSP structure modification. It was shown in shows the evolution of the monotonic plastic zone under LSP leads to the decreasing of plastic zone size combined with grain refinement with the shape of equiaxed grains even nanograins in the surface layer of materials [32-34]. This refinement provides more grain boundaries for impeding dislocation movement and increasing the difficulty for dislocations traversing grain boundaries.

Particular attention is paid to laser shock peening as the method of surface hardening for materials in the fine-grained states to eliminate the recrystallization factor in the conventional thermal treatment [35].

This work is devoted to studying the behavior of the Zr-1Nb alloy under laser induced shock-wave loading. Several works are devoted to the study of zirconium-based alloys during LSP [36-39]. The Zr-1Nb alloy is used for the manufacture of fuel element claddings for nuclear reactor fuel rods [40]. Therefore, this material is used in aggressive environmental conditions, including shock-wave (SW) loads. The behavior of this material under SW-loading was carried out in the works [40-42]. However, works devoted to the study of the Zr-1Nb alloy under SW loading in the ultrafine-grain (UFG) state have not been found in the literature. A significant increase in the strength characteristics of this material after severe plastic deformation is noted in the works [43-44]. In this regard, the idea of additional hardening of the Zr-1Nb alloy in the UFG state by LSP represents the interest.

Thus, the purpose of this work is to study the unique Zr-1Nb material in various structural states under laser-induced shock-wave loading.

MATERIAL

The Zr-1Nb alloy also known as E110 alloy in coarse-grained (CG) and ultrafine-grained states was studied. This is zirconium doped with 1% niobium. The UFG state was formed by the combined method of severe plastic deformation (SPD), which included free abs-pressing and multi-pass rolling in grooved rolls, followed by pre-recrystallization annealing. The specimens were annealed at a temperature of 580 °C for three hours in a vacuum before deformation processing. The CG state was obtained by recrystallization annealing of specimens in the UFG state. This unique material was provided by the Laboratory of Physics of Nanostructured Biocomposites of the Institute of Strength Physics and Materials Science of the Siberian Branch of Russian Academy of Sciences. The method of obtaining, mechanical testing, as well as structural studies of this material are presented in detail in the works [45-49].

EXPERIMENTAL STUDIES

The scheme of the experiment is shown in Fig. 1. The shock wave loading was carried out using a Beamtech SGR-Extra-10 high-energy nanosecond laser. The laser parameters were as follows: pulsed Nd: YAG laser; emission wavelength is 1064 nm; pulse energy up to 10 J; frequency is 1-5 Hz; pulse width is 11 +/- 1 ns; divergence: up to 3 mrad. The laser beam was focused on the target surface into a square spot with size of 1 mm. The fixture with the sample was mounted on a STEP SR50 industrial robotic 6-axis manipulator, which ensures the positioning accuracy of the sample relative to the laser is no worse than 0.1 mm. The velocity of the rear surface of the specimen was measured using a laser Doppler velocimeter (laser interferometer) FDVI Mark IV (VISAR - velocity interferometer system for any reflector). The used interferometer has the following technical characteristics: the radiation wavelength is 1550 nm; range of measured speeds from 15 to 15000 m/s; the error is 0.1%; time resolution from 0.8 to 50 ns (it depends on the range of measured speeds).

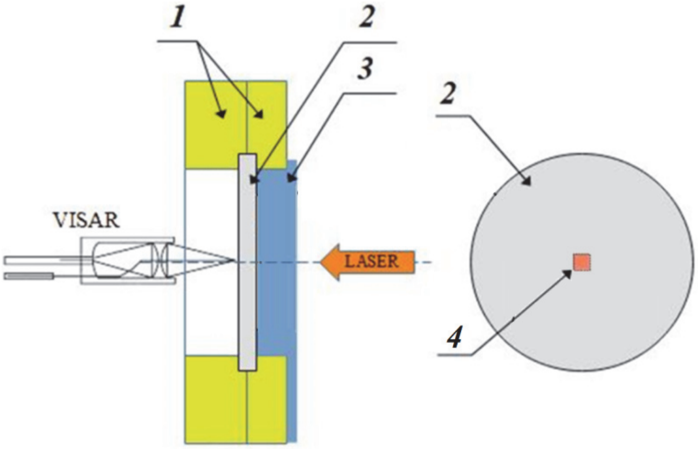

Figure 1: Scheme of the experiment. The numbers in the figure mean: 1 - detachable tooling for fixing the specimen; 2 - specimen; 3 - water curtain (laminar flow); 4 - laser impact zone.

A shock wave generated by a laser pulse that creates compressive stresses travels through the test sample material and is reflected from the rear surface. Tensile stresses are produced inside the sample material as a result of the interference of the incident and reflected waves, and their magnitude may be sufficient to cause damage to the material or even to build a circular plate. The optical part (objective) of the VISAR interferometer was mounted on a manipulator, on which a holder with a target-specimen was attached. This was done to ensure the accuracy of positioning and alignment of the beams of the loading laser and the VISAR measuring laser. The energy of the laser pulse in all experiments is 9.4 J. Specimen diameter is 13 mm. Other specimen parameters and characteristics measured in the experiment are shown in Tab. 1.

# State	h, mm	c_0, m/s	c_l, m/s	ρ_0, kg/m^3	σ_A, MPa	$\dot{\varepsilon}_A$, 10^6 1/s	σ_{HEL}, MPa	σ_{sp}, MPa	E, GPa
#1 CG	0.91	3024	3932	6404	1500	1.95	453	487	99
#2 CG	0.91				700	0.22	461	-	
#1 UFG	0.83	2411	2863	6222	900	0.64	377	-	51
#2 UFG	0.78				1000	3.36	374	325	

Table 1: Specimen parameters and mechanical characteristics of materials.

The signals received from the VISAR and oscilloscope systems were processed in a computer program [50]. Due to the specific loading conditions and due to the preparation of the sample surface, the type of velocity profiles varied from experiment to experiment. An example of the constructed profile is shown in Fig. 2.

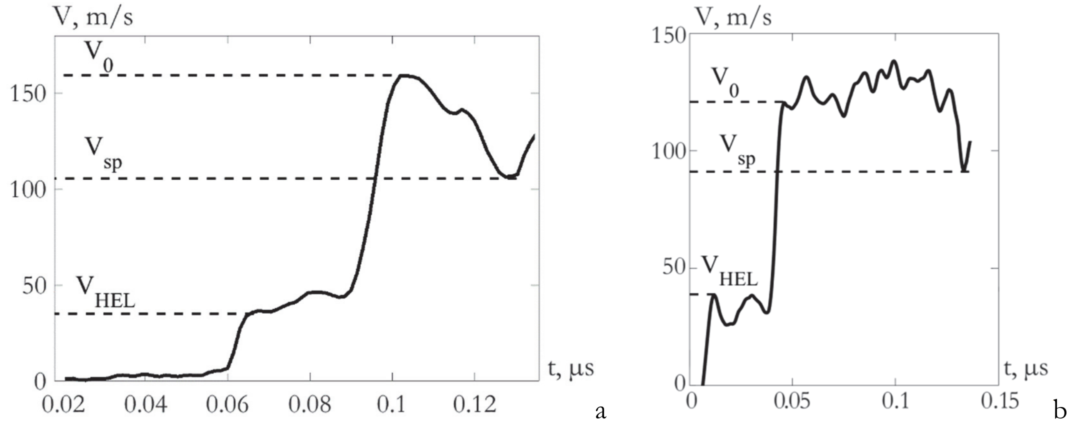

Figure 2: Free surface velocity profile for Zr-1Nb alloy in the CG (a) and UFG (b) state.

Physical and mechanical parameters of the studied materials are presented in Tab. 1. Young's modulus E was measured in work [49]. Initial mass density ρ_0 measured in this study. The longitudinal speed of sound c_l is calculated by the formula [51]:

$$c_l = \sqrt{\frac{E}{\rho_0}}$$

The volumetric speed of sound c_0 was estimated using the formula [51]:

$$c_0 = \frac{1}{\frac{\Delta t_1}{h_{sp}} - \frac{1}{c_l}}$$

where Δt_1 is the duration of the first pulse until the spall pulse front reaches the surface, which is determined on the free surface velocity profile; h_{sp} is the average thickness of the spall plate (the distance from the free surface of the target to the spall).

The amplitude of the compression pulse σ_A and the strain rate $\dot{\varepsilon}_A$ of the plastic front of the compression wave were determined from the velocity profiles of the free surface using the formulas [51]:

$$\sigma_A = 0.5 c_0 \rho_0 V_0$$

$$\dot{\varepsilon}_A = \frac{\Delta V}{\Delta t}\frac{1}{2c_0}$$

where V_0 is the velocity value at the first peak of the free surface velocity profile (Fig. 2); ΔV and Δt are increments of velocity and time on the linear section of the plastic front of the compression wave.

The dynamic Hugoniot elastic limit σ_{HEL} and the spall strength σ_{sp} were also determined from the free surface velocity profiles using the formulas [51]:

$$\sigma_{HEL} = 0.5 c_l \rho_0 V_{HEL}$$

$$\sigma_{sp} = 0.5 c_0 \rho_0 \left(V_0 - V_{sp} \right)$$

where V_{HEL} is the elastic precursor amplitude (Fig. 2); V_{sp} is the velocity reached before the spall pulse.

STRUCTURAL STUDIES

Before the start of the experiment, the surfaces of the samples were subjected to stepped mechanical grinding using sanding paper with a grain size from P320 to P2500 until a mirror surface was obtained. For the samples subjected to shock-wave loading, metallographic sections were produced in a plane perpendicular to the shock wave front to detect internal material defects (Fig. 3). The laser impact zone was in the plane of the metallographic section. The phases of material in the impact zone was examined with successive displacement of the cut plane occurring during repeated grinding and polishing in the direction affected area size (Fig. 3). Fig. 3 presents options for the potential development of interior damage to samples following shock-wave exposure.

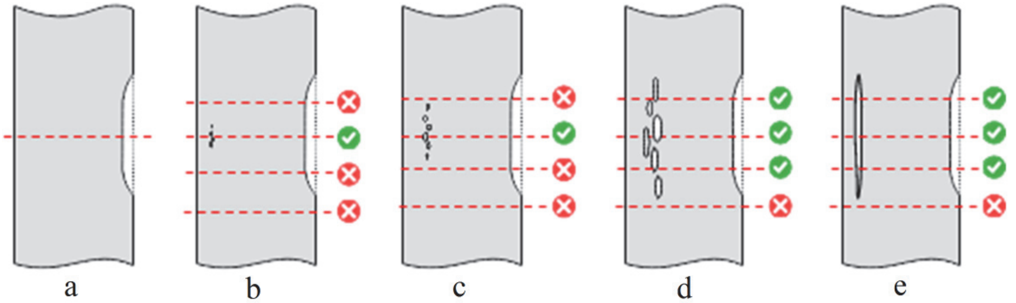

Figure 3: Variants of internal damage to the sample after shock-wave impact (a - no damage, b - single local damage of small size, c - accumulation of single damages; d - accumulation of large damages; e - single large damage.) and the probability of their detection depending on position of the plane of the metallographic section.

The formation of a single local discontinuity of the material (Fig. 3, b) due to the damage localization or extended damage localization areas (Fig. 3, c, d, e) as a result of the interference of the incident and reflected waves (spall failure).

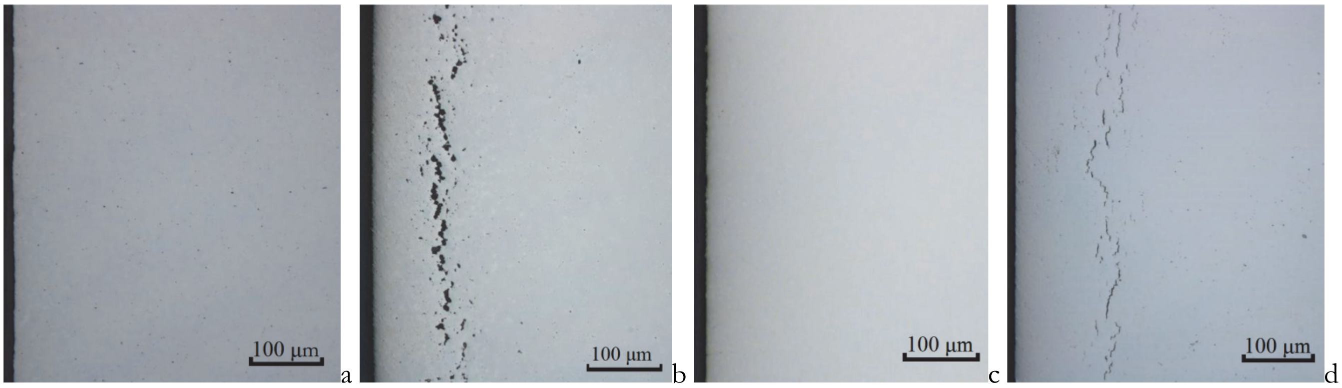

Figure 4: Characteristic types of the tested specimens of Zr-1Nb alloy CG state (a, b) and UFG state (c, d).

Fig. 4 (b) demonstrates that in the coarse grain (CG) state an internal damage zone can be seen forming in specimen at a distance of roughly 0.1 mm from the free surface of the specimen. Large-sized pores have accumulated to generate this structure. This zone is around 0.7 mm long overall. There are specimens as well where no indications of internal damage were discovered (Fig. 4, a). There are also indications of spall failure for the material in the UFG state (Fig. 4, d). It should be noticed that the developed zone of internal damage measures around 0.9 mm in length and is situated approximately 0.13 mm from the specimen's free surface. This damage has a different morphology from those in the CG state of the material. These are not a build-up of big pores, but rather a build-up of tiny, twisting fractures. Probably the differing structural state of the material is to blame for this occurrence.

Internal damage was found on the specimen in the CG state and on the specimen in the UFG state. Spall failure was not detected on other specimens. This fact raises the question: why was a different result obtained under the "same" loading conditions? One possible explanation is the following. Ensuring a constant and uniform laminar fluid flow over the target surface is impossible in the above scheme (Fig. 1) due to the loading features. The loading pulse is formed due to the formation of plasma, which appears due to ablation due to laser exposure. The amplitude and shape of the loading pulse may vary significantly from experiment to experiment due to the very short exposure time. The amplitudes of the compression pulses and the characteristic strain rates obtained from the profiles of the free surface prove this assumption. The amplitudes of strain rates in specimens with observed spalling are many times greater than in specimens without spalling (Tab. 1). The compression pulse amplitudes are also higher. Thus, the loading conditions are not known for certain. Numerical simulation of the process under study was carried out in order to have an approximate idea of the amplitudes of the loading pulse. And also, to find out the conditions under which spalling occurs or does not occur.

NUMERICAL SIMULATION

A model based on the statistical theory of defects [52] is applied to simulate the damage-failure transition under Laser Shock loading according to the statement by [53-55] using the set of the balance equations and constitutive relations in the following form:

$$\varrho\dot{\mathrm{v}} = \nabla \cdot \boldsymbol{\sigma} \tag{1}$$

$$\dot{\varrho} + \varrho\nabla \cdot \mathrm{v} = 0 \tag{2}$$

$$\mathrm{D} = \frac{1}{2}\left(\nabla\mathrm{v} + \nabla\mathrm{v}^{T}\right) \tag{3}$$

$$\boldsymbol{\sigma} = \boldsymbol{\sigma}_{s} + \boldsymbol{\sigma}_{d}\,, \boldsymbol{\sigma}_{s} = \frac{1}{3}\boldsymbol{\sigma} : \mathrm{E} \tag{4}$$

$$\boldsymbol{\sigma}^{R} = \lambda\left(\mathrm{D} : \mathrm{E}\right)\mathrm{E} + 2G(\mathrm{D} - \dot{\boldsymbol{\varepsilon}}^{p} - \dot{\mathrm{p}}) \tag{5}$$

$$\boldsymbol{\sigma}^{R} = \dot{\boldsymbol{\sigma}} - \dot{\mathbf{R}} \cdot \mathbf{R}^{T} \cdot \boldsymbol{\sigma} + \boldsymbol{\sigma} \cdot \dot{\mathbf{R}} \cdot \mathbf{R}^{T} \tag{6}$$

$$\dot{\boldsymbol{\varepsilon}}^{p} = \dot{\varepsilon}_{0}^{n_{\varepsilon}}(\Gamma_{\sigma}\boldsymbol{\sigma} - \Gamma_{p\sigma}\frac{\partial F}{\partial \mathbf{p}}) \tag{7}$$

$$\dot{\mathrm{p}} = \dot{\varepsilon}_{0}^{n_{p}}(\Gamma_{p\sigma}\boldsymbol{\sigma} - \Gamma_{p}\frac{\partial F}{\partial \mathrm{p}}) \tag{8}$$

$$\frac{F}{F_{m}} = \frac{p^{2}}{2} - \frac{p^{2}}{2\delta} + c_{1}p + c_{2}\ln(c_{3} + c_{4}p + p^{2}) - \frac{\boldsymbol{\sigma}_{d} : \mathrm{p}}{2G} \tag{9}$$

where: ϱ is the mass density; $\boldsymbol{v}$ is the velocity vector; $\boldsymbol{\sigma}$ is the stress tensor; ∇ is the nabla operator; «·» is the scalar product; $\boldsymbol{D}$ is the velocity strain tensor; $\boldsymbol{\sigma}_s$ and $\boldsymbol{\sigma}_d$ are the spherical and deviatoric parts of the stress tensor; «:» is the double scalar product; $\boldsymbol{E}$ is the unit tensor; $(\cdot)^R$ is the Green-Naghdi derivative, R-derivative; λ, G are the elastic material constants; $\boldsymbol{\varepsilon}^p$ is the plastic strain tensor; $\boldsymbol{p}$ is the tensor of microshears density, which in its physical sense is the strain induced by defects; $(\cdot)^T$ is the transposition operation; $\boldsymbol{R}$ is the orthogonal tensor of the polar expansion of the deformation gradient; n_ε, n_p are the constants responsible for the rate sensitivity of the material; Γ_σ, $\Gamma_{\sigma p}$, Γ_p are the kinetic coefficients, material constants; F is the free energy; δ is the structural scaling parameter; c_1-c_4, F_m are the approximation constants.

The material constants of the model are determined according to the developed experimental-numerical procedure [53]. Constants Γ_σ, $\Gamma_{\sigma p}$, Γ_p are defined by the solution of problem of minimizing the deviation between the experimental and calculated stress-strain diagrams under quasi-static loading. Experimental stress-strain diagrams from the work [48] were used. An illustration of the solution is shown in Fig. 5.

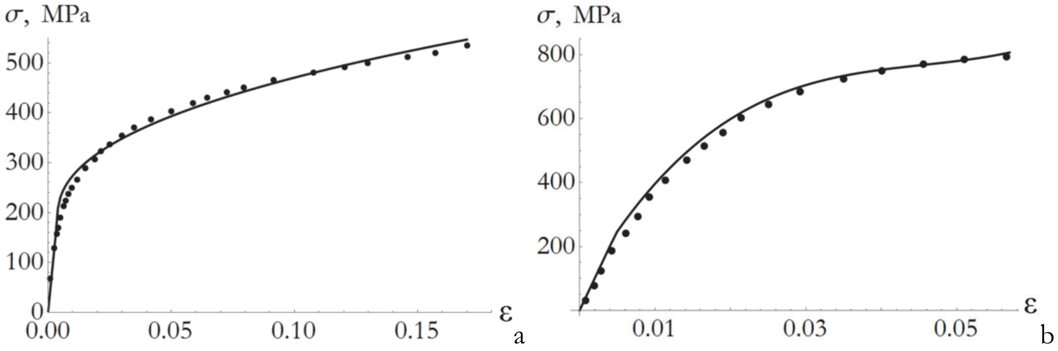

Figure 5: Stress-strain diagrams for the Zr-1Nb alloy in the CG and UFG states. The calculation is indicated by a solid line. Dots are experimental data [48].

Dynamic yield strength data was used to determine the constants responsible for the rate sensitivity of the material. Hugoniot elastic limit was used to estimate the dynamic yield strength by the relation [51]:

$$\sigma_Y = 1.5\sigma_{HEL}\left[1-\left(\frac{c_b}{c_l}\right)^2\right]$$

The complete set of material constants is presented in Tab. 2.

Parameter	CG-state	UFG-state
λ	49 GPa	48 GPa
G	39 GPa	19 GPa
ϱ	6404 kg/m^3	6222 kg/m^3
Γ_σ	$4.53\cdot10^{-9}$ (Pa·s)$^{-1}$	$1.47\cdot10^{-9}$ (Pa·s)$^{-1}$
$\Gamma_{\sigma p}$	$0.32\cdot10^{-9}$ (Pa·s)$^{-1}$	$0.62\cdot10^{-9}$ (Pa·s)$^{-1}$
Γ_p	$0.02\cdot10^{-9}$ (Pa·s)$^{-1}$	$0.03\cdot10^{-9}$ (Pa·s)$^{-1}$
n_ε	0.975	0.99
n_p	0.975	0.99
δ	1.15	1.4
c_1	−0.00535972	−0.00535972
c_2	0.519	0.519
c_3	0.581	0.581
c_4	0.006	0.006

Table 2: Material parameters.

The failure criterion $\sigma_{eq} \geq \sigma_{sp}$ was used, where σ_{eq} is the equivalent von Mises stress, σ_{sp} is the spall strength (values are presented in Tab. 1).

The problem was solved numerically for axi-symmetric case by the finite element method (FEM). The loading conditions are shown schematically in Fig. 6. The radius of the laser pulse area was taken equal to 0.5 mm, which corresponds to the experiment. Shock-wave loading, which is a consequence of laser exposure, was simulated by setting a triangular pressure pulse with a duration of 50 ns (Fig. 6). It was shown in [12] that the pressure pulse loading the specimen under the action of a laser has a duration of ~100 ns. This time is longer than the characteristic effect of the laser itself. The symmetry conditions are set on the lower boundary of the computational domain. It is depicted by the dotted line in Fig. 6. The free surface conditions are set on the remaining boundaries of the computational domain. The Abaqus software was used for numerical calculations. Elements of the CAX4R type were used in the calculation: 4-node bilinear axisymmetric quadrilateral, reduced integration, hourglass control. The size of the elements was chosen so that there were 1000 elements along the length of the target. The mesh was divided into 200 segments along the radius to reduce the estimated time. It is shown that such a partition is sufficient. Macroscopic fracture is implemented by removing elements from the computational domain in which the failure criterion is reached. In this case, a new free surface is formed at the place of removal of the element.

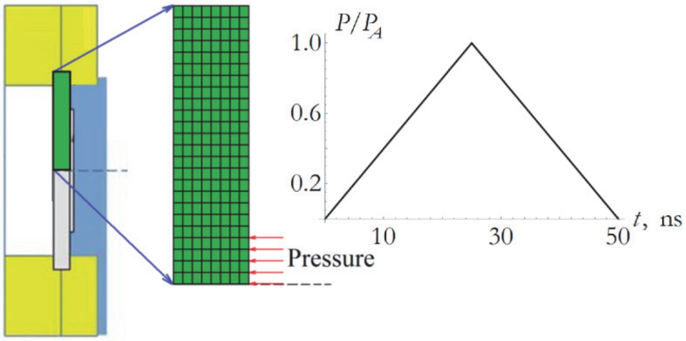

Figure 6: The geometry of the problem and the loading conditions.

The calculation on a sample 1 mm thick with a loading pulse amplitude of 1 GPa was carried out first. These conditions, as the authors see, are most consistent with the conditions of the experiment. Calculations for all states of the material showed the absence of spall fracture. Then the amplitude was substantially increased up to 50 GPa. Multiple damage inside the specimen is observed at this amplitude, however, spalling does not occur (Fig. 7, a). The situation in which a part of the target has been torn off, for example, as shown in Fig. 7 (c), is called a "spalling" in this context. However, it must be understood that spalling is unlikely for the specified geometry, since the target diameter is much larger than the impact diameter. Therefore, the detachment of a part of the specimen is possible only with a very powerful impact. The failure scenario seen in Fig. 7 (a) cannot be considered physical. First, the loading conditions are clearly higher than those realized in the experiment. Secondly, the intensity of the impact is such that it goes beyond the applicability of the model used. Therefore, the hypothetical amplitude of the loading pulse was reduced to 10 GPa. Spalling does not occur, but internal damage is observed (Fig. 7, b) at this amplitude. This damage scenario is qualitatively similar to the situation observed in the experiment.

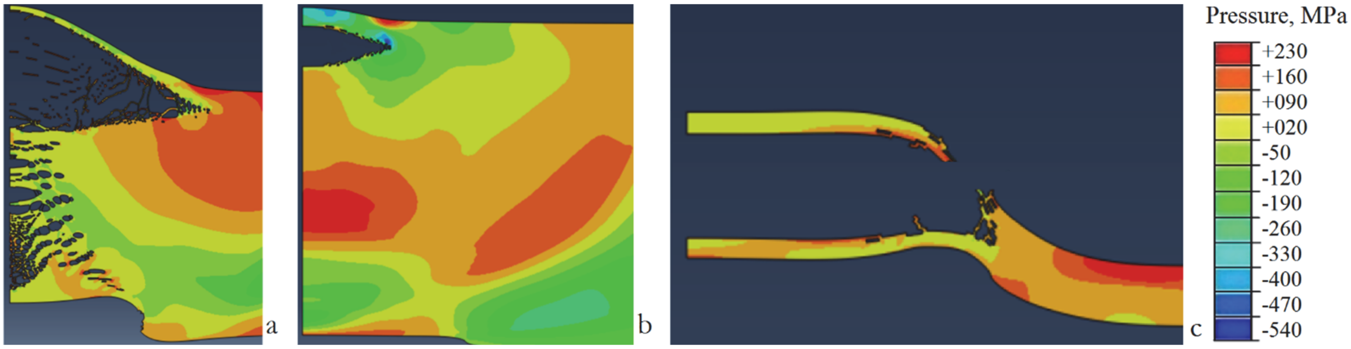

Figure 7: Results of numerical calculations for CG state. a - the sample thickness is 1 mm, the pulse amplitude is 50 GPa, b - the sample thickness is 1 mm, the pulse amplitude is 10 GPa, c - the sample thickness is 0.1 mm, the pulse amplitude is 10 GPa

Comparison of results for UFG and CG states is shown in Fig. 8. Modeling qualitatively predicts an increase in the length of the damage region under the same loading conditions (target thickness 1 mm, pulse amplitude 10 GPa). The length of the damage zone turned out to be 0.53 mm for the CG state and 0.66 mm for the UFG state.

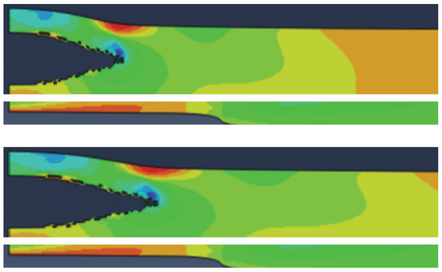

Figure 8: Comparison of damage region length for UFG and CG states. The top picture is the CG state. Bottom picture is the UFG state.

Finally, the calculation with an amplitude of 3 GPa was carried out. None of the above calculations led to the detachment of part of the target. Therefore, calculations with smaller thicknesses were carried out to identify this possibility. The calculations were carried out for all states. All results are shown in Tabs. 3 and 4. The situation in which spalling occurs at a sample thickness of 0.1 mm and a pulse amplitude of 10 GPa is the most physical.

Pressure amplitude / Target thickness	1 GPa	3 GPa	10 GPa	50 GPa
1 mm	No damage	Internal damage	Internal damage	Multiple internal damage. No spall fracture
0.3 mm	Internal damage	Internal damage	Internal damage	Spall fracture
0.1 mm	Internal damage	Internal damage	Spall fracture	The target has been broken

Table 3: Simulation results for CG state.

Pressure amplitude / Target thickness	1 GPa	3 GPa	10 GPa	50 GPa
1 mm	No damage	Internal damage	Internal damage	Multiple internal damage. No spall fracture
0.3 mm	Internal damage	Internal damage	Spall fracture	Spall fracture
0.1 mm	Internal damage	Internal damage	Spall fracture	The target has been broken

Table 4: Simulation results for UFG state.

THE DISCUSSION OF THE RESULTS

The empirical dependence of the spall strength of the Zr-1Nb alloy in the CG state on the characteristic strain rate was obtained in [40]: $\sigma_{sp} = 40.2 \cdot 10^{6} \cdot \dot{\varepsilon}^{0.164}$. The spall strength varies in the range from 388 MPa to 505 MPa for the range of strain rate from 10^{6} s^{-1} to $5 \cdot 10^{6}$ s^{-1}. These values are in good agreement with the result obtained in the present study (σ_{sp} = 487 MPa, $\dot{\varepsilon}_{A}$ = 1,95·10^{6} s^{-1}). It should be understood that the amplitude of the strain rate at the plastic front and the characteristic strain rate during spalling are not the same value. However, these quantities are of the same order. In addition, another way of loading and initiating shock waves was used in the work [40]. Thus, the reliability of the results obtained is confirmed by the correspondence with the results of other authors.

It is shown that the dynamic elastic limit for the CG state is higher than for the UFG state. The spall strength for the CG state is also higher. It was shown in [48] that the ultimate strength under quasi-static loading for the Zr-1Nb alloy in the

UFG state is higher than for the CG state. It is difficult to compare static yield strengths. This is due to the fact that it is problematic to determine the yield strength for the UFG material from its loading diagram (Fig. 5, b). However, the average plastic flow stress for the UFG state is clearly higher than for the CC state. Thus, we can conclude that the Zr-1Nb alloy in the UFG state is more susceptible to fracture at high strain rate (~10^6 s^{-1}), including spall fracture during LSP, despite the higher strength characteristics under quasi-static loading. The longer section of the destruction area also confirms this fact. However, the greater length of the damage zone can be caused by the smaller specimen thickness, since the radius of influence decreases as it goes deeper into the target. At the same time, numerical simulation showed a qualitative increase in the radius of the damage zone for the same thicknesses for the UFG material. Therefore, an increase in the size of the damage region for the UFG state may result from a combination of two factors. Damage, including micropores and microcracks, accumulates in the material during severe plastic deformation. A significant decrease in the Young's modulus is also explained by a significant accumulation of damage. Naimark [54, 56] showed that it is micropores and microcracks that are the type of defects that make a decisive contribution to spalling formation. Perhaps the reason why the Zr-1Nb alloy in the UFG state, obtained by the method described in [49], has reduced strength characteristics at high strain rate.

The observed internal damages differ for the CG and UFG states. The characteristic damage size is larger for the CG state. Perhaps this is due to the different characteristic sizes of the structural elements. Despite the lower value of the spall strength, the nature of the damage for the UFG material is apparently less critical for the strength of the specimen (structure) as a whole.

The failure scenarios obtained in numerical calculations turned out to be so due to the specifics of the implementation of macroscopic failure. A more physical scenario of destruction, which would be more like an experiment, cannot be obtained in this case. A single large crack does not look like what is shown in Fig. 4 (b, d). However, if we continue the calculation and let the system come to a state of equilibrium, then the resulting picture would be much more plausible. The problem is that such a calculation takes orders of magnitude more time. This is due to the fact that the characteristic relaxation times are orders of magnitude longer than the exposure times. Therefore, such a calculation is impossible. However, some qualitative matches were obtained. Internal damage that does not come to the surface, as in the experiment, is observed. The length (radius) of this damage area is not quantitatively described. In this formulation, that was impossible, because the shape and amplitude of the loading pulse are unknown. Based on the goals of modeling, it can be concluded that the range of amplitudes of the loading pulse, which is formed under laser exposure, is in the range from 1 to 3 GPa. Spall fracture at the indicated ratio of the diameter and the area of laser impact is possible only with a sufficiently small sample thickness (0.1 mm) and an unnaturally large amplitude of the loading pulse (10 GPa). Thus, such a phenomenon will not occur during laser shock peening. But the appearance of internal damage is quite possible.

CONCLUSIONS

The physical and mechanical characteristics of the Zr-1Nb alloy in the CG and UFG states under shock-wave loading have been obtained. It is shown that the dynamic elastic limit and spall strength in the CG state are higher. The value of the dynamic elastic limit is ~460 MPa for the coarse-grained state and ~370 MPa for the ultrafine-grained state. The spall strength is ~490 MPa and ~330 MPa, respectively. Thus, the Zr-1Nb alloy in the UFG state is more susceptible to spall fracture, including LSP.

Approximate amplitudes of the loading pulse generated by the laser action are established by means of numerical simulation. The conditions under which spall fracture will occur have been identified. It is shown that internal spall damage does not occur at loading pulse amplitudes less than 1 GPa. The effect of increasing the damage area for the UFG state in comparison with the CG state under the same loading conditions is qualitatively described.

AUTHOR CONTRIBUTIONS

- Sergey Uvarov: experiment on laser exposure.
- Aleksandr Balakhnin: preparation of specimrns before the experiment, structural studies.
- Irina Bannikova: signal processing from VISAR; construction of free surface velocity profiles; calculation of the mechanical characteristics of the material obtained in the experiment.

- Oleg Naimark: conceptualization; supervision, project administration and funding acquisition; author of the statistical theory of defects; proposed the structure of the constitutive relations of the used mathematical model.
- Yuriy Bayandin: specification of the potential of nonequilibrium free energy approximation in the model used.
- Dmitry Ledon: modification of the model used to take into account the strain rate sensitivity of the material; identification of model constants; carrying out numerical calculations; analysis of results.

ACKNOWLEDGEMENTS

This research was supported by the Russian Science Foundation (project 21-79-30041), https://rscf.ru/en/project/21-79-30041/

REFERENCES

[1] Seddik, R., Rondepierre, A., Prabhakaran S., Morin L., Favier V., Palin-Luc T., Berthe L. (2022) Identification of constitutive equations at very high strain rates using shock wave produced by laser, European Journal of Mechanics - A/Solids, 92, pp. 104432. DOI: 10.1016/j.euromechsol.2021.104432.

[2] Lu, J.Z., Xue, K.N., Lu, H.F., Xing, F., Luo, K.Y. (2021) Laser shock wave-induced wear property improvement and formation mechanism of laser cladding Ni25 coating on H13 tool steel, Journal of Materials Processing Technology, 296, pp. 117202. DOI: 10.1016/j.jmatprotec.2021.117202.

[3] Wu, J., Zhao, J., Qiao, H., Hu, X., Yang Y. (2020) The New Technologies Developed from Laser Shock Processing, Materials, 13(6), pp. 1453. DOI: 10.3390/ma13061453.

[4] Zhang, Z. et. al. (2023) Progress in applications of shockwave induced by short pulsed laser on surface processing, Optics & Laser Technology, 157, pp. 108760. DOI: 10.1016/j.optlastec.2022.108760.

[5] Wang, Z.D., Sun, G.F., Lu, Y., Chen, M.Z., Bi, K.D., Ni, Z.H. (2020) Microstructural characterization and mechanical behavior of ultrasonic impact peened and laser shock peened AISI 316L stainless steel, Surface and Coatings Technology, 385, pp. 125403. DOI: 10.1016/j.surfcoat.2020.125403.

[6] Kolobov, Yu.R., Manokhin, S.S, Betekhtin, V.I., Kadomtsev, A.G., Narykova, M.V., Odintsova, G.V., Khramov, G.V. (2022). Investigation of the effect of nanosecond laser pulses processing on the microstructure and fatigue resistance of commercially pure titanium, Technical Physics Letters, 48, pp. 56-59.

[7] Bai, Y. et. al. (2021) Life cycle strengthening of high-strength steels by nanosecond laser shock, Applied Surface Science, 569, pp. 151118. DOI: 10.1016/j.apsusc.2021.151118.

[8] Gachegova, E.A., Sikhamov, R., Ventzke, V., Kashaev, N., Plekhov, O.A. (2022) Influence of laser shock peening on low- and high-cycle fatigue of an OT4-0 titanium alloy, Journal of Applied Mechanics and Technical Physics, 63 (2), pp. 335–342. DOI:10.1134/S0021894422020171.

[9] Peyre, P., Fabbro, R. (1995) Laser shock processing: A review of the physics and applications, Opt. Quantum Electron, 27 (12), pp. 1213–1229. DOI: 10.1007/BF00326477.

[10] Kostina, A. et. al. (2022) Finite-element study of residual stress distribution in Ti-6Al-4V alloy treated by laser shock peening with varying parameters, Frattura ed Integrita Strutturale, 16(61), pp. 419–436. DOI:10.3221/IGF-ESIS.61.28.

[11] Mironov, S. et. al. (2022) On the relationship between microstructure and residual stress in laser-shock-peened Ti-6Al-4V, Journal of Alloys and Compounds, 900, pp. 163383. DOI: 10.1016/j.jallcom.2021.163383.

[12] Plekhov, O.A., Kostina, A.A., Iziumov, R.I., Iziumova, A.Yu. (2022) Finite-element analysis of residual stresses in the TC4 titanium alloy treated by laser shock peening, Computational Continuum Mechanics, 15(2), pp. 171–184. DOI:10.7242/1999-6691/2022.15.2.13

[13] Qi, S., Bao, H., Shen, Y. (2022) Numerical investigation on spall fracture in a metallic material caused by laser shock peening, Materials Today Communications, 33, pp. DOI: 104343. 10.1016/j.mtcomm.2022.104343.

[14] Ruschau, J., John, R., Thompson, S.R., Nicholas, T. (1999) Fatigue crack nucleation and growth rate behavior of laser shock peened titanium, Int. J. Fatigue, 21, pp. 199–209. DOI: 10.1016/S0142-1123(99)00072-9.

[15] Liu, Q., Barter, S., Clark, G. (2002) Internal cracking during surface treatment of 7050-t74 aluminium alloy using laser shock peening, Int. Conf. Struct. Integrity Fract., 25, pp. 177–182.

[16] Pan, X. et. al. (2023) Microstructure and residual stress modulation of 7075 aluminum alloy for improving fatigue performance by laser shock peening, International Journal of Machine Tools and Manufacture, 184, pp. 103979. DOI: 10.1016/j.ijmachtools.2022.103979.

[17] He, Z. et. al. (2021) Laser shock peening regulating aluminum alloy surface residual stresses for enhancing the mechanical properties: Roles of shock number and energy, Surface and Coatings Technology, 421, pp. 127481. DOI: 10.1016/j.surfcoat.2021.127481.

[18] Wang, J. et. al. (2019) Mechanical properties and microstructural response of 2A14 aluminum alloy subjected to multiple laser shock peening impacts, Vacuum, 165, pp. 193-198. DOI: 10.1016/j.vacuum.2019.03.058.

[19] Wu, J., Zou, S., Zhang, Y., Sun, G., Ni, Z., Cao, Z., Che, Z. (2018) Spall of Ti17 alloy induced by laser shock peening with multiple shots, Explos. Shock Waves, 38 (5), pp. 1091–1098. DOI: 10.11883/bzycj-2017-0082.

[20] Fang, Y. (2021) Strengthening characteristics in TC17 titanium alloy treated during LSP, Optik, 226, pp. 165895. DOI: 10.1016/j.ijleo.2020.165895.

[21] Sun, R. et. al. (2017) Dynamic response and residual stress fields of Ti6Al4V alloy under shock wave induced by laser shock peening, Modelling Simul. Mater. Sci. Eng., 25, pp. 065016. DOI 10.1088/1361-651X/aa7a46.

[22] Eliezer, S., Gilath, I., Bar-Noy, T. (1990) Laser-induced spall in metals: Experiment and simulation, J. Appl. Phys., 67 (2), pp. 715–724, DOI: 10.1063/1.345777.

[23] Boustie, M., Cottet, F. (1991) Experimental and numerical study of laser induced spallation into aluminum and copper targets, J. Appl. Phys., 69 (11), pp. 7533–7538. DOI: 10.1063/1.347570

[24] Righi, G., Ruestes, C.J., Stan, C.V., Ali, S.J., Rudd, R.E., Kawasaki, M., Park, H.-S., Meyers, M.A. (2021) Towards the ultimate strength of iron: spalling through laser shock, Acta Mater., 215, pp.117072, DOI: 10.1016/j.actamat. 2021.117072.

[25] Zhang, L., Huang, Y., Shu, H., Chen, B., Chen, X., Ma, Y., Liu, W. (2022) Spallation damage of 90W-Ni-Fe alloy under laser-induced plasma shock wave, J. Mater. Res. Technol., 17, pp. 1731-1739. DOI: 10.1016/j.jmrt.2022.01.090.

[26] Wu, J., Zou, S., Gong, S., Cao, Z., Che, Z., Sun, R. (2020) Over peening effect of Al7050 mid-thick plates with continued multiple laser shock peening impacts at the same position, Rare Met. Mater. Eng., 49 (10), pp. 3395–3401.

[27] Sun, R., Li, L., Guo, W., Peng, P., Zhai, T., Che, Z., Li, B., Guo, C., Zhu, Y. (2018) Laser shock peening induced fatigue crack retardation in Ti-17 titanium alloy, Materials Science & Engineering A, 737, pp. 94-104. DOI: 10.1016/j.msea.2018.09.016.

[28] Lin, B., Lupton, C., Spanrad, S., Schofield, J., Tong, J. (2014) Fatigue crack growth in lasershock-peened Ti–6Al–4V aerofoil specimens due to foreign object damage, Int. J. Fatigue, 59, pp. 23–33. DOI: 10.1016/j.ijfatigue.2013.10.001.

[29] Nowell, D., Duó, P., Stewart, I.F. (2003) Prediction of fatigue performance in gas turbine blades after foreign object damage, Int. J. Fatigue, 25, pp. 963–969. DOI: 10.1016/S0142-1123(03)00160-9.

[30] Sheng, J., Huang, S., Zhou, J.Z., Lu, J.Z., Xu, S.Q., Zhang, H.F. (2016) Effect of laser peening with different energies on fatigue fracture evolution of 6061-T6 aluminum alloy, Opt. Laser Technol., 77, pp. 169–176. DOI: 10.1016/j.optlastec.2015. 09.008.

[31] Kashaev, N., Ventzke, V., Horstmann, M., Chupakhin, S., Riekehr, S., Falck, R., Maawad, E., Staron, P., Schell, N., Huber, N. (2017) Effects of laser shock peening on the microstructure and fatigue crack propagation behaviour of thin AA2024 specimens, Int. J. Fatigue, 98, pp. 223–233. DOI: 10.1016/j.ijfatigue.2017.01.042.

[32] Lu, J.Z., Wu, L.J., Sun, G.F., Luo, K.Y., Zhang, Y.K., Cai, J., Cui, C.Y., Luo, X.M. (2017) Microstructural response and grain refinement mechanism of commercially pure titanium subjected to multiple laser shock peening impacts, Acta Mater., 127, pp. 252–266. DOI: 10.1016/j.actamat.2017.01.050.

[33] Lu, J.Z., Luo, K.Y., Zhang, Y.K., Cui, C.Y., Sun, G.F., Zhou, J.Z., Zhang, L., You, J., Chen, K.M., Zhong, J.W. (2010) Grain refinement of LY2 aluminum alloy induced by ultrahigh plastic strain during multiple laser shock processing impacts, Acta Mater., 58, pp. 3984–3994. DOI: 10.1016/j.actamat.2010.03.026.

[34] Lu, J.Z., Deng, W.W., Luo, K.Y., Wu, L.J., Lu, H.F. (2017) Surface EBSD analysis and strengthening mechanism of AISI304 stainless steel subjected to massive LSP treatment with different pulse energies, Mater. Charact., 125, pp. 99-107. DOI: 10.1016/j.matchar.2017.01.036.

[35] Kolobov, Y.R., Manokhin, S.S., Betekhtin, V.I., Kadomtsev, A.G., Narykova, M.V., Odintsova, G.V. (2021) Studying the influence of nanosecond pulsed laser action on the structure of submicrocrystalline titanium, Technical Physics Letters, 47, pp. 721–725. DOI: 10.1134/S1063785021070245.

[36] Mahmoud, Z.H., Barazandeh, H., Mostafavi, S.M., Ershov, K., Goncharov, A., Kuznetsov, A.S., Kravchenko, O.D., Zhu, Yu. (2021) Identification of rejuvenation and relaxation regions in a Zr-based metallic glass induced by laser shock peening, Journal of Materials Research and Technology, 11, pp. 2015-2020. DOI: 10.1016/j.jmrt.2021.02.025.

[37] Fu, J. et. al. (2014) Effect of laser shock peening on mechanical properties of Zr-based bulk metallic glass, Applied Surface Science, 313, pp. 692-697. DOI: 10.1016/j.apsusc.2014.06.056.

[38] Liang, M. et. al. (2018) Effect of laser shock peening and its size-dependence on the compressive plasticity of Zr-based bulk metallic glass, Journal of Materials Processing Technology, 251, pp. 47-53. DOI: 10.1016/j.jmatprotec.2017.08.013.

[39] Luo, S. et. al. (2019) The compound process of laser shock peening and vibratory finishing and its effect on fatigue strength of Ti-3.5Mo-6.5Al-1.5Zr-0.25Si titanium alloy, Journal of Alloys and Compounds, 783, pp. 828-835. DOI: 10.1016/j.jallcom.2018.12.294.

[40] Kazakov, D.N., Kozelkov, O.E., Maiorova, A.S., Malyugina, S.N., Mokrushin, S.S., Pavlenko, A.V. (2014) Dynamic properties of zirconium alloy E110 under shock-wave loading of submicrosecond duration, Mechanics of Solids, 49 (6), pp. 657-665. DOI: 10.3103/S0025654414060077.

[41] Taluts, N.I., Dobromyslov, A.V., Kozlov, E.A. (2009) Structure and phase state of Zr-1% Nb and zZr-2.5% Nb alloys loaded by spherically converging shock waves, The Physics of Metals and Metallography, 108 (2), pp. 171-178. DOI: 10.1134/S0031918X09080109.

[42] Taluts N., Dobromyslov A., Kozlov E. (2009) Structural and phase transformations in Zr and Zr-Nb alloys under loading by spherical converging stress waves, International Journal of Materials Research, 100 (3), pp. 362-365. DOI: 10.3139/146.110024.

[43] Legostaeva, E.V., Sharkeev, Y.P., Eroshenko, A.Y., Belyavskaya, O.A., Uvarkin, P.V., Vavilov, V.P., Chulkov, A.O., Skrypnyak, V.A., Klopotov, A.A., Kozulin, A.A., Skrypnyak, V.V., Ustinov, A.M. (2021) Influence of Zr-1 wt.% Nb alloy structure state on its deformation and thermal behavior under quasi-static tension, Materials Letters, 285. pp. 129028. DOI: 10.1016/j.matlet.2020.129028.

[44] Sharkeev, Y.P., Legostaeva, E.V., Belyavskaya, O.A., Eroshenko, A.Y., Vavilov, V.P., Chulkov, A.O., Skripnyak, V.A., Kozulin, A.A., Skripnyak, V.V., Kuznetsov, V.P., Zhilyakov, A.Y., Skorobogatov, A.S. (2019) Infrared thermography and generation of heat under deformation of bioinert titanium- and zirconium-based alloys, Russian Journal of Nondestructive Testing, 55 (7), pp. 533-541. DOI: 10.1134/S1061830919070076.

[45] Eroshenko, A.Y., Sharkeev, Y.P., Khimich, M.A., Uvarkin, P.V., Tolmachev, A.I., Glukhov, I.A., Legostaeva, E.V. (2021) Effect of prolonged thermal exposure on microstructure and mechanical properties of Zr – 1 wt.% Nb and Ti – 45 wt.% Nb ultrafine-grained bioinert alloys, Russian Physics Journal, 63 (11), pp. 1846-1853. DOI: 10.1007/s11182-021-02242-4.

[46] Sharkeev, Y.P., Vavilov, V.P., Chulkov, A.O., Kuimova, M.V., Legostaeva, E.V., Eroshenko, A.Y., Belyavskaya, O.A., Skrypnyak, V.A., Klopotov, A.A., Kozulin, A.A., Skrypnyak, V.V., Zhilyakov, A.Y., Kouznetsov, V.P., Ustinov, A.M. (2020) Research on the processes of deformation and failure in coarse- and ultrafine-grain states of Zr1–Nb alloys by digital image correlation and infrared thermography, Materials Science and Engineering: A, 784, pp. 139203. DOI: 10.1016/j.msea.2020.139203.

[47] Legostaeva, E.V., Sharkeev, Y.P., Belyavskaya, O.A., Eroshenko, A.Y., Vavilov, V.P., Skripnyak, V.A., Zhilyakov, A.Y., Kuznetsov, V.P. (2021) The influence of ultrafine-grained state of Zr – 1 wt.% Nb and Ti – 45 wt.% Nb alloys on their thermophysical properties and energy dissipation and accumulation during deformation, Russian Physics Journal, 63 (11), pp. 1867-1875. DOI: 10.1007/s11182-021-02270-0.

[48] Sharkeev, Y.P., Legostaeva, E.V., Belyavskaya, O.A., Eroshenko, A.Y., Glukhov, I.A., Vavilov, V.P., Chulkov, A.O., Skripnyak, V.A., Kozulin, A.A., Skripnyak, V.V. (2019) Regular features of stage formation in the stress-strain curves and microstructure in the zone of fracture of coarse-grained and ultrafine-grained titanium and zirconium alloys, Russian Physics Journal, 62 (8), pp. 1349-1356.

[49] Eroshenko, A.Yu., Mairambekova, A.M., Sharkeev, Yu.P., Kovalevskaya, Zh.G., Khimich, M.A., Uvarkin, P.V. (2017) Structure, phase composition and mechanical properties in bioinert zirconium-based alloy after severe plastic deformation, Letters on Materials, 7 (4), pp. 469-472. DOI: 10.22226/2410-3535-2017-4-469-472.

[50] Bannikova, I., Uvarov, S., Bayandin, Yu., Naimark, O. (2014) An experimental study of non-Newtonian properties of water under electroexplosive loading. Technical Physics Letters, 40, pp. 766-768. DOI: 10.1134/S1063785014090041.

[51] Kanel, G., Razorenov, S., Utkin, A., Fortov V. (2008) Experimental profiles of shock waves in condensed substances, Moscow, Fizmatlit. (In Russian).

[52] Naimark, O.B. (2003) Collective properties of defects ensembles and some nonlinear problems of plasticity and fracture, Physical mesomechanics, 6, pp. 39-63.

[53] Bayandin, Yu.V., Ledon, D.R., Uvarov, S.V. (2021) Verification of wide-range constitutive relations for elastic-viscoplastic materials using the Taylor–Hopkinson test, Journal of Applied Mechanics and Technical Physics, 62, pp. 1267-1276. DOI: 10.1134/S0021894421070026.

[54] Bayandin, Y., Saveleva, N., Naimark, O. (2019) Steady plastic wave fronts and scale universality of strain localization in metals and ceramics, Frattura ed Integrita Strutturale, 13 (49), pp. 243-256. DOI: 10.3221/IGF-ESIS.49.24.

[55] Bannikov, M., Bilalov, D., Oborin, V., Naimark O. (2019) Damage evolution in the AlMg6 alloy during high and very high cycle fatigue, Frattura ed Integrita Strutturale, 13 (49), pp. 383-395. DOI: 10.3221/IGF-ESIS.49.38.

[56] Naimark, O., Bayandin, Y., Uvarov, S., Bannikova, I., Saveleva, N. (2021) Critical dynamics of damage-failure transition in wide range of load intensity, Acta Mechanica, 232 (5), pp. 1943-1959.
DOI: 10.1007/s00707-020-02922-1.